

Distribution Grid Optimal Power Flow in Unbalanced Multiphase Networks With Volt-VAr and Volt-Watt Droop Settings of Smart Inverters

Adedoyin Inaolaji , Graduate Student Member, IEEE, Alper Savasci , Graduate Student Member, IEEE, and Sumit Paudyal , Member, IEEE

Abstract—High penetration of photovoltaic (PV) generators in active distribution networks (ADNs) cause overvoltage due to reverse power flow. Smart inverter (SI) functionalities can be configured to provide efficient voltage regulation and reactive power support in ADNs. Moreover, the mismatch between peak PV generation and peak demand make battery energy storage systems (BESSs) increasingly important assets in power grids, capable of enabling higher penetration of renewable energy resources by mitigating the system-wide effects of PV intermittency. In this work, we propose the inclusion of local piecewise Volt-VAr and Volt-Watt droop functions of PV (as per the IEEE-1547) as constraints in a multiperiod distribution grid optimal power flow (DOPF) formulation. This approach is an efficient voltage control method for unbalanced multiphase networks, making the inverter dispatch solutions abide by the IEEE-1547 standard and therefore suitable at the local inverter controller level. We adopt a well-known LinDist3Flow version of DOPF, and the resulting multiperiod DOPF becomes a mixed-integer linear programming problem. Simulations on the IEEE 123-node feeder with 15 utility-scale PV and BESS inverters validate the efficacy of the proposed formulation in performing effective voltage regulation and control that abide by the IEEE-1547 standard. The case studies show that SI droop-integrated DOPF can ensure reduced variation in bus voltages, reducing the risk of voltage violations, and net load smoothing can be achieved with BESS, reducing the disparity between inexpensive midday and expensive evening energy price.

Index Terms—Distribution grids, droop settings, energy storage, IEEE-1547, mixed-integer linear programming (MILP), optimal power flow, photovoltaic (PV), smart inverter (SI).

NOMENCLATURE

Sets and Indices

\mathcal{B}	Set of buses in the distribution system.
\mathcal{L}	Set of lines (branches) in the distribution system.

Manuscript received 31 July 2021; revised 22 December 2021 and 13 March 2022; accepted 4 May 2022. Date of publication 9 June 2022; date of current version 25 August 2022. This work was supported by National Science Foundation under Grant ECCS-2001732. Paper 2021-PSEC-0943.R2, presented at the 2021 Industry Applications Society Annual Meeting, Vancouver, BC, Canada, Oct. 10–14, and approved for publication in the IEEE TRANSACTIONS ON INDUSTRY APPLICATIONS by the Power Systems Engineering Committee of the IEEE Industry Applications Society. (*Corresponding author:* Adedoyin Inaolaji.)

The authors are with the Department of Electrical and Computer Engineering, Florida International University, Miami, FL 33199 USA (e-mail: ainao003@fiu.edu; asava014@fiu.edu; spaudyal@fiu.edu).

Color versions of one or more figures in this article are available at <https://doi.org/10.1109/TIA.2022.3181110>.

Digital Object Identifier 10.1109/TIA.2022.3181110

$i \in \mathcal{B}$	Bus index, where $i = \{0, 1, 2, \dots, n\}$ for $n + 1$ buses.
$(i, j) \in \mathcal{L}$	Branch index, also denoted as $i \rightarrow j$.
\mathcal{T}	Set of time intervals.
$t \in \mathcal{T}$	Time index, where $t = \{1, 2, \dots, T\}$ for T time intervals.
\mathcal{B}^G	Set of buses with PVs.
\mathcal{B}^B	Set of buses with BESS.
\mathcal{B}'	Set of buses excluding the substation bus.
ψ	Phases in the network, where $\psi \subseteq \{a, b, c\}$.
ϕ	Alias of ψ .
Ψ_i	Set of phases of bus $i \in \mathcal{B}$, where $\psi \in \Psi_i$.
Ψ_{ij}	Set of phases of branch $(i, j) \in \mathcal{L}$, where $\psi \in \Psi_{ij}$.
Φ_i, Φ_{ij}	Alias of Ψ_i and Ψ_{ij} , respectively.
l	Index of breakpoints used in modeling piecewise SI droop curves, where $l = \{1, 2, \dots, w\}$ for w breakpoints in the droop curve.
<i>Parameters</i>	
α	Ratio of voltage phasors.
z_{ij}	Impedance matrix of branch $(i, j) \in \mathcal{L}$.
γ	Angle utilized in the polyhedral approximation.
\mathbb{H}_{ij}	Modified impedance matrix derived for active power flow for branch (i, j) .
\mathbb{M}_{ij}	Modified impedance matrix derived for reactive power flow for branch (i, j) .
k	Half the number of polygon vertices in the polyhedral approximation.
$r_{ij}^{\psi\phi}, x_{ij}^{\psi\phi}$	Resistance and reactance values between phase ψ of bus i and phase ϕ of bus j of branch $(i, j) \in \mathcal{L}$, respectively.
Δt	Time resolution.
$\eta_{i,\text{CHA}}^{\psi}, \eta_{i,\text{DIS}}^{\psi}$	Charging and discharging efficiencies, respectively.
$\underline{\text{SOC}}_i^{\psi}, \overline{\text{SOC}}_i^{\psi}$	Minimum and maximum SOCs of BESS at phase $\psi \in \Psi_i$ of bus $i \in \mathcal{B}^B$, respectively.
\underline{v}, \bar{v}	Magnitude-squared of minimum and maximum voltage limits, respectively.
$p_{i,L}^{\psi}, q_{i,L}^{\psi}$	Active and reactive power load demands at phase $\psi \in \Psi_i$ of bus $i \in \mathcal{B}$, respectively.

$q_{i,C}^\psi$	Reactive power injected by capacitor at phase $\psi \in \Psi_i$ of bus $i \in \mathcal{B}$.
$\bar{E}_{i,\text{BESS}}^\psi$	Maximum state-of-charge of BESS located at phase $\psi \in \Psi_i$ of bus $i \in \mathcal{B}^B$.
$\bar{p}_{i,\text{BESS}}^\psi$	Active power rating of BESS at phase $\psi \in \Psi_i$ of bus $i \in \mathcal{B}^B$, based on the solar irradiation and PV active power rating.
$\bar{p}_{i,G}^\psi$	Maximum active power that can be injected by PV at phase $\psi \in \Psi_i$ of bus $i \in \mathcal{B}^G$, based on the solar irradiation and PV active power rating.
$\bar{q}_{i,G}^\psi$	Maximum reactive power that can be injected by SI at phase $\psi \in \Psi_i$ of bus $i \in \mathcal{B}^G$.
$\bar{s}_{i,\text{BESS}}^\psi$	Apparent power rating of BESS located at phase $\psi \in \Psi_i$ of bus $i \in \mathcal{B}^B$.
$\bar{s}_{i,G}^\psi$	Apparent power rating of SI at phase $\psi \in \Psi_i$ of bus $i \in \mathcal{B}^G$.
<i>Variables</i>	
V_i^ψ	Complex voltage at bus i for phase $\psi \in \Psi_i$.
u_i^ψ	Voltage magnitude at bus i for phase $\psi \in \Psi_i$, i.e., $u_i^\psi = V_i^\psi $.
\mathbf{V}_i	Vector of all available phase ψ complex voltage at bus i , i.e., $\mathbf{V}_i := [V_i^\psi]_{\psi \in \Psi_i}$.
v_i^ψ	Magnitude-squared of voltage at bus i for phase $\psi \in \Psi_i$, i.e., $v_i^\psi := V_i^\psi ^2$.
I_{ij}	Vector of sending-end complex current flowing on branch $(i, j) \in \mathcal{L}$.
P_{ij}^ψ, Q_{ij}^ψ	Sending-end active and reactive powers flowing on phase $\psi \in \Psi_{ij}$ of branch $(i, j) \in \mathcal{L}$, respectively.
S_{ij}	$S_{ij} = P_{ij} + \mathbf{j}Q_{ij}$ is the vector of sending-end complex power flowing on branch $(i, j) \in \mathcal{L}$.
p_i^ψ, q_i^ψ	Active and reactive power net injections at phase $\psi \in \Psi_i$ of bus $i \in \mathcal{B}$, respectively.
s_i	$s_i = p_i + \mathbf{j}q_i$ is the complex power net injection vector at bus $i \in \mathcal{B}$.
$p_{i,\text{DIS}}^\psi$	Discharging rate of BESS located at phase $\psi \in \Psi_i$ of bus $i \in \mathcal{B}^B$ at the grid interface.
$\beta_{i,l}$	Variables used in modeling piecewise droop curves.
$\text{SOC}_i^{\psi,t}$	SOC of BESS at phase $\psi \in \Psi_i$ of bus $i \in \mathcal{B}^B$ during time $t \in \mathcal{T}$.
$e_{i,l}$	Indicator variables for each pair of adjacent variables $(\beta_{i,l}, \beta_{i,l+1})$ at node $i \in \mathcal{B}$, used in modeling piecewise droop curves.
$p_{i,\text{CHA}}^\psi$	Charging rate of BESS located at phase $\psi \in \Psi_i$ of bus $i \in \mathcal{B}^B$ at the grid interface.
$p_{i,G}^\psi, q_{i,G}^\psi$	Active and reactive power injections by SI at phase $\psi \in \Psi_i$ of bus $i \in \mathcal{B}^G$, respectively.
$q_{i,\text{BESS}}^\psi$	Reactive power provided by BESS located at phase $\psi \in \Psi_i$ of bus $i \in \mathcal{B}^B$.
$p_{\text{sub}}^\psi, q_{\text{sub}}^\psi$	Active and reactive power injection vectors at the substation, i.e., at phase $\psi \in \Psi_i$ of bus $i \in \{0\}$, respectively.

I. INTRODUCTION

A. Background and Motivation

Distributed energy resources (DERs) are being increasingly adopted worldwide due to several factors, including the flexibility they provide to grid operations. Among the renewable DERs, photovoltaic (PV) generation is the fastest growing power generation system and has increased significantly in the recent decade [1]. Since power distribution grids have limited DER hosting capacity at a particular time of the day, significant uptake of PV generation can have negative impacts, such as reverse power flow and voltage rise and fluctuations [2]. Voltage control is, therefore, a vital function performed by the distribution management system (DMS), which is tasked with developing effective control strategies to ensure that local service voltages are maintained within the American National Standards Institute (ANSI) range.

With revised IEEE-1547 standard [3], DERs are allowed to provide voltage regulation support through droop-based active and reactive power control in response to changes in voltage at the point of common coupling (PCC). The value of IEEE-1547 is that it helps to standardize modern DER performance capabilities to enable the power system to transition from just accommodating these DERs to integrating them as grid assets. In this regard, smart inverter (SI) features are becoming an injunction (e.g., California's Rule 21 [4] and Hawaii's Rule 14H [5]) with subsequent compliance testing of SI governed by the UL 1741 SA. Unlike traditional inverters, which disconnect during overvoltage occurrences, SIs can continue operation via their advanced self-governing and adaptation features under a wide range of voltage and frequency disturbances [6]. In addition, SIs can provide ancillary grid support, such as voltage as, well as frequency regulation through droop-based local control functions, such as Volt-VAr, Volt-Watt, and frequency-Watt, which can autonomously adjust the active and/or reactive power output of inverters within a specified voltage range as per IEEE-1547 guided-droop functions [7]. Specifically, combining reactive power support [via Volt-VAr functionality, i.e., $\mathbf{Q}(\mathbf{V})$] with active power curtailment [via Volt-Watt functionality, i.e., $\mathbf{P}(\mathbf{V})$] can provide valuable solutions for overvoltage mitigation and maximization of PV hosting capacity, especially as the share of PV resources in the grid increases [8].

Since SI functionalities are becoming an essential part of the distributed PV operations, reliable and collective utilization of inverter functions requires utilities to enhance their existing DMS applications. Integrating such functionalities requires sufficient abstraction and systematic modeling of each inverter function within DMS decision making processes. Existing DMS applications extensively use distribution grid optimal power flow (DOPF)-based approaches for operational and planning purposes. In [9]–[11], DOPF was used to dispatch active and reactive power of controllable devices for the purpose of loss minimization and mitigation of voltage violations in power distribution grids. However, the SIs are required to operate based on local droop settings as per the IEEE-1547 [3], and the existing DOPF models do not incorporate the droop setting

of SIs. Therefore, the setpoints obtained from DOPF could violate local droop settings rendering these DOPF-based methods unsuitable at the local inverter controller level. In order to ensure system-level optimality and prevent dispatch solutions that may violate IEEE-1547, it becomes inevitable to incorporate SI local droop functionalities in the DOPF models.

Moreover, the significant uptake of intermittent renewable energy resources leads to a mismatch between peak PV generation and peak demand. In this regard, the optimal dispatch of battery energy storage systems (BESSs) are essential assets in power grids that are capable of enabling higher penetration of renewable energy resources by mitigating the system-wide effects of PV intermittency and enhancing resource adequacy [12]. BESS is usually connected to distribution grids through power electronic converters, acting as an active power source and sink, and providing additional reactive power capability when required. In this work, we propose the inclusion of local piecewise Volt-VAr and Volt-Watt droop functions (as per the IEEE-1547) as constraints in the DOPF formulation for unbalanced multiphase networks.

B. Related Work

Integration of $\mathbf{Q}(\mathbf{V})$ and $\mathbf{P}(\mathbf{V})$ functions within a DOPF framework is challenging, as the DOPF in its original form is a nonlinear and nonconvex problem, posing limitations in terms of poor scalability and intractability of the DOPF model. This has led to the development of several linear approximations and convex relaxations [13]. In [14], $\mathbf{Q}(\mathbf{V})$ and $\mathbf{P}(\mathbf{V})$ droop functionalities were integrated into a linear model for coordinated inverter control. In [8], we formulated the exact Volt-VAr and Volt-Watt functions within a DOPF.

Additional computational challenges are presented by the piecewise linear nature of the $\mathbf{Q}(\mathbf{V})$ and $\mathbf{P}(\mathbf{V})$ droops. In [15], big-M method modeling of the piecewise-linear relation of $\mathbf{Q}(\mathbf{V})$ function was combined with a second-order cone programming (SOCP) grid model to obtain a mixed-integer SOCP (MISOCP) formulation. Detailed analysis is further carried out on the approximation of first-order voltage term from the squared of the voltage magnitude used in the convex MISOCP formulation. The models in the abovementioned works (see [8], [14], and [15]) were applied to single-phase circuits and can also be extended to phase-decoupled multiphase circuits, where the multiphase circuits are decoupled into single-phase circuits by ignoring the mutual coupling of phases. Distribution systems, however, require consideration of multiphase structure with the inclusion of mutual coupling. In [16], a sequential quadratic programming was used to obtain optimal settings of $\mathbf{Q}(\mathbf{V})$ and $\mathbf{P}(\mathbf{V})$ in a multiphase network. In [17], a standard piecewise Volt-VAr droop function was integrated into a linearized DOPF formulation to dispatch various control assets in an unbalanced distribution network. Only Volt-VAr droop functions of SIs were considered with limited analysis of droop curve operation. However, distribution systems are characterized by a high R/X ratio, making active power injections to be more sensitive to voltage variations; hence, it is more beneficial to combine both Volt-VAr and Volt-Watt functionalities [8].

C. Contributions

The contributions of this article are as follows.

- 1) We present a reformulation of local piecewise linear droop functions of Volt-VAr and Volt-Watt capabilities in mixed-integer linear form utilizing the *lambda method* [18].
- 2) The mixed-integer $\mathbf{P}(\mathbf{V})$ and $\mathbf{Q}(\mathbf{V})$ models are integrated as constraints to a *LinDist3Flow* model [19], along with a generic BESS model, which significantly extends our previous study [8]. Although it ignores losses, the *LinDist3Flow* model is formulated for multiphase modeling and has been shown to yield reasonably accurate results compared to its phase-decoupled counterparts [20]. We utilize Taylor series expansion (TSE) to solve the first-order voltage approximation problem. The resulting DOPF formulation then becomes a mixed-integer linear programming (MILP) model. The quadratic constraint introduced as a result of the simultaneous control of active and reactive power of PV is convexified by polyhedral linearization. The DOPF model is found to be effective in dispatching setpoints that exactly align with $\mathbf{P}(\mathbf{V})$ and $\mathbf{Q}(\mathbf{V})$ droops defined in the IEEE-1547 and, along with the BESS, can actively participate in the regulation of the distribution system voltage.

This article improves our earlier efforts of integrating SI droop functions in DOPF [8], [15], [16], [21], [22] in the following ways.

- 1) First, the integration of the Volt-VAr and Volt-Watt droop functionalities into DOPF is analyzed within the context of a multiphase unbalanced DOPF with consideration of phase-coupling.
- 2) Second, the integration of BESS introduces time interdependencies or intertemporal constraints, which further complicate the DOPF model and show the computational effectiveness of the proposed models.

The rest of this article is organized as follows. Section II describes the operating region of the PV inverter and details the mathematical formulations for modeling the distribution grid. Section III presents the proposed mathematical modeling of the SI droop functions using the *lambda method*. Section IV presents the BESS model within a multiperiod DOPF framework, the objective considered, and the overall DOPF model integrating Volt-VAr and Volt-Watt droops. The test system setup and case studies are presented in Section V. Discussion and analysis of simulation results are provided in Section VI. Finally, Section VII concludes this article.

II. MATHEMATICAL MODELS AND PRELIMINARIES

A. PV Inverter Control

A PV system consists of a group of solar panels that receive insolation from the sun and convert a dc signal to an ac signal through a power-electronics-based inverter. The inverter is capable of a two-quadrant operation, providing reactive power compensation through injection and absorption of reactive power, as shown in Fig. 1. Reactive power is delivered to the grid during the injection operation, and the PV system acts as a capacitive

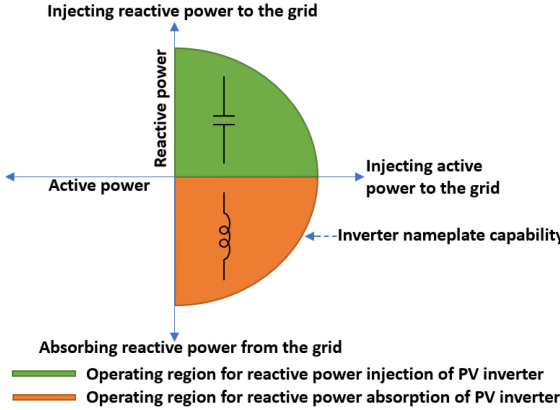


Fig. 1. Operating regions for the PV inverter.

generator with a leading power factor. On the other hand, the PV system acts as an inductive generator during the absorption operation, and reactive power is taken from the grid at a lagging power factor. The inverter is not a limitless source or sink of reactive power; instead, its reactive power capability is bounded by its fixed apparent power nameplate rating and the variable active power, expressed mathematically by

$$\sqrt{(p_{i,G}^\psi)^2 + (q_{i,G}^\psi)^2} \leq \bar{s}_{i,G}^\psi \quad \forall i \in \mathcal{B}^G \quad \forall \psi \in \Psi_i. \quad (1)$$

Given that both $p_{i,G}^\psi$ and $q_{i,G}^\psi$ are controllable, then (1) is a nonconvex constraint. This can be convexified and approximated by making use of a 32-vertex polygon ($k = 16$) and defining a polyhedral norm [23] as

$$\begin{aligned} -\bar{s}_{i,G}^\psi &\leq \cos(l\gamma) p_{i,G}^\psi + \sin(l\gamma) q_{i,G}^\psi \leq \bar{s}_{i,G}^\psi \\ \gamma &= \frac{\pi}{k}, \quad l = 1, \dots, k \quad \forall i \in \mathcal{B}^G \quad \forall \psi \in \Psi_i. \end{aligned} \quad (2)$$

The following box constraints ensure the active and reactive power capabilities:

$$0 \leq p_{i,G}^\psi \leq \bar{p}_{i,G} \quad \forall i \in \mathcal{B}^G \quad \forall \psi \in \Psi_i \quad (3)$$

$$-\bar{q}_{i,G} \leq q_{i,G}^\psi \leq \bar{q}_{i,G} \quad \forall i \in \mathcal{B}^G \quad \forall \psi \in \Psi_i. \quad (4)$$

B. Distribution Grid Model

Distribution networks are characteristically unbalanced because of untransposed lines, unbalanced loading scenarios, and multiphase feeds (see [24, Ch. 2]). Therefore, it becomes imperative to model the coupling effects across multiple phases. In this regard, let a radial unbalanced distribution network be represented by a directed graph consisting of a set of \mathcal{B} buses and a set of \mathcal{L} branches connecting these buses.

In a three-phase network, the power flow is modeled by the following set of branch flow model (BFM) equations [25]:

$$\mathbf{V}_i - \mathbf{V}_j = \mathbf{z}_{ij} \mathbf{I}_{ij} \quad \forall (i, j) \in \mathcal{L} \quad (5a)$$

$$\mathbf{S}_{ij} = \mathbf{V}_i \mathbf{I}_{ij}^* \quad \forall (i, j) \in \mathcal{L} \quad (5b)$$

$$\mathbf{s}_j = \sum_{k:j \rightarrow k} \mathbf{S}_{jk} - \sum_{i:i \rightarrow j} (\mathbf{S}_{ij} - \mathbf{z}_{ij} \mathbf{I}_{ij}) \quad \forall j \in \mathcal{B}. \quad (5c)$$

Equation (5) represents a nonlinear formulation in the BFM, and it includes the mutual coupling among the phases. Hence, it is an exact representation of the distribution grid.

In [19], the ratio of voltage phasors was approximated by constants as

$$V_i^a (V_i^b)^{-1} \approx \alpha, \quad V_i^b (V_i^c)^{-1} \approx \alpha, \quad V_i^a (V_i^c)^{-1} \approx \alpha^2 \quad (6)$$

where $\alpha = 1 \angle 120^\circ = \frac{-1+j\sqrt{3}}{2}$ and $\alpha^2 = 1 \angle 240^\circ = -\frac{1+j\sqrt{3}}{2}$.

By decomposing the well-known BFM [25] into real and imaginary terms of phase quantities, ignoring the loss term and incorporating the assumption in (6), the following linear equations are derived:

$$p_j^\psi = \sum_{k:j \rightarrow k} P_{jk}^\psi - \sum_{i:i \rightarrow j} P_{ij}^\psi \quad \forall j \in \mathcal{B} \quad \forall \psi \in \Psi_j \quad (7a)$$

$$q_j^\psi = \sum_{k:j \rightarrow k} Q_{jk}^\psi - \sum_{i:i \rightarrow j} Q_{ij}^\psi \quad \forall j \in \mathcal{B} \quad \forall \psi \in \Psi_j \quad (7b)$$

$$\begin{aligned} v_i^\psi &= v_j^\psi - \mathbb{H}_{ij}^{\psi\phi} P_{ij}^\phi - \mathbb{M}_{ij}^{\psi\phi} Q_{ij}^\phi \\ \forall (i, j) \in \mathcal{L} \quad \forall \psi \in \Psi_{ij} \quad \forall \phi \in \Phi_{ij} \end{aligned} \quad (8)$$

where

$$\mathbb{H}_{ij} = \begin{bmatrix} -2r_{ij}^{aa} & r_{ij}^{ab} - \sqrt{3}x_{ij}^{ab} & r_{ij}^{ac} + \sqrt{3}x_{ij}^{ac} \\ r_{ij}^{ba} + \sqrt{3}x_{ij}^{ba} & -2r_{ij}^{bb} & r_{ij}^{bc} - \sqrt{3}x_{ij}^{bc} \\ r_{ij}^{ca} - \sqrt{3}x_{ij}^{ca} & r_{ij}^{cb} + \sqrt{3}x_{ij}^{cb} & -2r_{ij}^{cc} \end{bmatrix} \quad (9a)$$

$$\mathbb{M}_{ij} = \begin{bmatrix} -2x_{ij}^{aa} & x_{ij}^{ab} + \sqrt{3}r_{ij}^{ab} & x_{ij}^{ac} - \sqrt{3}r_{ij}^{ac} \\ x_{ij}^{ba} - \sqrt{3}r_{ij}^{ba} & -2x_{ij}^{bb} & x_{bc} + \sqrt{3}r_{ij}^{bc} \\ x_{ij}^{ca} + \sqrt{3}r_{ij}^{ca} & x_{ij}^{cb} - \sqrt{3}r_{ij}^{cb} & -2x_{ij}^{cc} \end{bmatrix}. \quad (9b)$$

The *LinDist3Flow* formulation is thus modeled by (7)–(9) [19]. We adopt *LinDist3Flow* model because it comprehensively considers mutual coupling between phases and yields more accurate results compared to phase-decoupled counterparts [20].

The convention of positive sign for power injection and negative sign for power extraction is assumed. At the substation, the net injection is

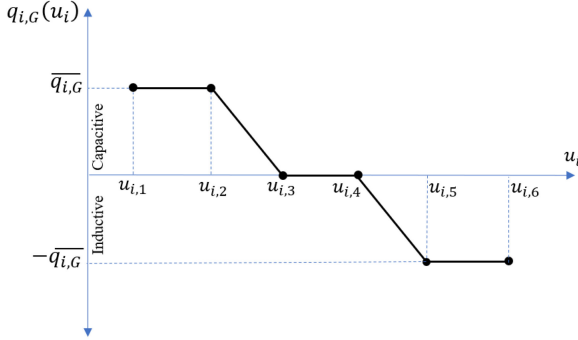
$$p_i^\psi = p_{\text{sub}}^\psi + p_{i,G}^\psi + p_{i,\text{DIS}}^\psi + p_{i,\text{CHA}}^\psi - p_{i,L}^\psi \quad \forall i \in \{0\} \quad \forall \psi \in \Psi_i \quad (10a)$$

$$q_i^\psi = q_{\text{sub}}^\psi + q_{i,G}^\psi + q_{i,\text{BESS}}^\psi + q_{i,C}^\psi - q_{i,L}^\psi \quad \forall i \in \{0\} \quad \forall \psi \in \Psi_i. \quad (10b)$$

At other buses excluding the substation, the net injection is

$$\begin{aligned} p_i^\psi &= p_{i,G}^\psi + p_{i,\text{DIS}}^\psi + p_{i,\text{CHA}}^\psi - p_{i,L}^\psi \\ \forall i \in \mathcal{B}' \quad \forall \psi \in \Psi_i \end{aligned} \quad (11a)$$

$$\begin{aligned} q_i^\psi &= q_{i,G}^\psi + q_{i,C}^\psi + q_{i,\text{BESS}}^\psi - q_{i,L}^\psi \\ \forall i \in \mathcal{B}' \quad \forall \psi \in \Psi_i. \end{aligned} \quad (11b)$$

Fig. 2. Typical five-segment $Q(V)$ droop curve of SI [3].

If a PV system, BESS, capacitor, or load is not installed at a particular bus, the corresponding entry will become zero in (10) and (11). Note that $p_{i,CHA}^\psi$ can only take negative values [refer to (20c)], while $p_{i,DIS}^\psi$ can only take positive values [refer to (20d)].

The system voltages are expected to be maintained within acceptable ANSI limits to achieve voltage regulation. This is depicted by

$$\underline{v} \leq v_i^\psi \leq \bar{v} \quad \forall i \in \mathcal{B}' \quad \forall \psi \in \Psi_i. \quad (12)$$

III. PROPOSED MODELING OF SI DROOP FUNCTIONS

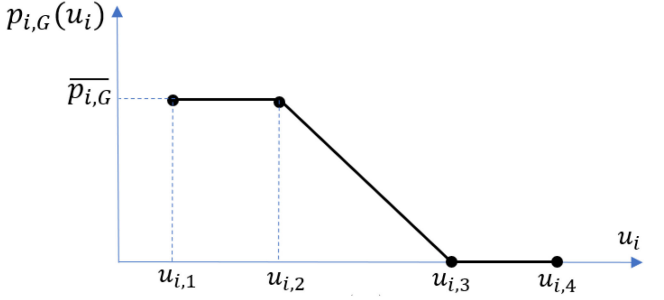
This section presents the mathematical modeling of SI droop curves, as defined in the IEEE-1547. The per-phase grid support functionalities are shown, but we omit the phase superscripts in this section for brevity.

A. Volt-VAr Droop Function of PV

The $Q(V)$ configuration, as shown in Fig. 2, defines a continuous, univariate, and piecewise linear relationship between VAr generation and system voltage at the PCC. When the observed voltage is between $u_{i,1}$ and $u_{i,2}$, the maximum available reactive power is injected into the grid, whereas when the observed voltage is between $u_{i,2}$ and $u_{i,3}$, reactive power is injected into the grid as a function of the slope. On the other hand, when the PCC voltage is between $u_{i,4}$ and $u_{i,5}$, the SI absorbs the reactive power based on the slope, whereas when the PCC voltage is between $u_{i,5}$ and $u_{i,6}$, the SI absorbs the maximum available reactive power. A deadband occurs between $u_{i,3}$ and $u_{i,4}$ in which no reactive power compensation is applied when the PCC voltage is within this range.

The mathematical representation of $Q(V)$ droop curve can be written as the following piecewise function:

$$q_{i,G}(u_i) = \begin{cases} +\overline{q}_{i,G}, & u_{i,1} \leq u_i \leq u_{i,2} \\ \frac{-\overline{q}_{i,G}}{u_{i,3}-u_{i,2}} u_i + \frac{\overline{q}_{i,G} u_{i,3}}{u_{i,3}-u_{i,2}}, & u_{i,2} < u_i \leq u_{i,3} \\ 0, & u_{i,3} < u_i \leq u_{i,4} \\ \frac{-\overline{q}_{i,G}}{u_{i,5}-u_{i,4}} u_i + \frac{\overline{q}_{i,G} u_{i,4}}{u_{i,5}-u_{i,4}}, & u_{i,4} < u_i \leq u_{i,5} \\ -\overline{q}_{i,G}, & u_{i,5} < u_i \leq u_{i,6} \end{cases} \quad \forall i \in \mathcal{B}^G. \quad (13)$$

Fig. 3. Typical three-segment $P(V)$ droop curve of SI [3].

An epigraph $q_{i,G}(u_i) \leq d$ can be modeled as

$$u_i = \sum_{l=1}^w \beta_{i,l} u_{i,l}, \quad \sum_{l=1}^w \beta_{i,l} q_{i,G}(u_{i,l}) \leq d \quad \forall i \in \mathcal{B}^G. \quad (14)$$

The condition that only two adjacent variables can be nonzero is also called an special ordered sets of type 2 (SOS2) constraint. Using the *lambda method* [18], an SOS2 constraint is then modeled in mixed-integer linear form as

$$\left. \begin{array}{l} \beta_{i,1} \leq e_{i,1}, \\ \beta_{i,l} \leq e_{i,l} + e_{i,l-1}, \quad l = 2, \dots, w-1, \\ \beta_{i,w} \leq e_{i,w-1}, \quad \beta \geq 0, \\ \sum_{l=1}^w \beta_{i,l} = 1, \quad \sum_{l=1}^{w-1} e_{i,l} = 1, \quad e \in \{0, 1\}^{w-1} \end{array} \right\} \forall i \in \mathcal{B}^G. \quad (15)$$

B. Volt-Watt Droop Function of PV

The $P(V)$ droop control, as shown in Fig. 3, controls PV active power output. The PV injects its maximum available active power when the PCC voltage lies within the range of $u_{i,1}$ and $u_{i,2}$. For a PCC voltage between $u_{i,2}$ and $u_{i,3}$, the PV active power output is curtailed based on the steepness of the slope. A deadband occurs where no active power is injected for PCC voltage between $u_{i,3}$ and $u_{i,4}$.

The mathematical representation of $P(V)$ droop curve can be written as the following piecewise function:

$$p_{i,G}(u_i) = \begin{cases} \overline{p}_{i,G}, & u_{i,1} \leq u_i \leq u_{i,2} \\ \frac{-\overline{p}_{i,G}}{u_{i,3}-u_{i,2}} u_i + \frac{\overline{p}_{i,G} u_{i,3}}{u_{i,3}-u_{i,2}}, & u_{i,2} < u_i \leq u_{i,3} \\ 0, & u_{i,3} < u_i \leq u_{i,4} \end{cases} \quad \forall i \in \mathcal{B}^G. \quad (16)$$

Similar to the modeling of $Q(V)$ droop curve, SOS2 constraint is enforced for piecewise representation of $P(V)$ droop as in (14) and (15).

C. First-Order Voltage Approximation

Integrating Volt-VAr and Volt-Watt droops into the base *LinDist3Flow* presents a challenge in that, while the droop functions use the first-order of voltage magnitude, i.e., u_i , in modeling the droop curve, the base *LinDist3Flow-DOPF* model utilizes the square of the voltage magnitude, i.e., v_i . Therefore,

it is necessary to consider the relationship of $v_i = u_i^2$ in the DOPF formulation when the droop curves are incorporated to the base *LinDist3Flow*-DOPF model. However, imposing this quadratic relationship as an exact constraint will lead to a nonlinear nonconvex formulation, which may be intractable. Since the piecewise droops are modeled with integer variables, then the intuitive choice would be to retain the MILP formulation by reformulating constraint $v_i = u_i^2$ as a linear or mixed-integer linear constraint.

Although other approximation or linearization techniques (as done in [15] and [21]) can be applied to the quadratic voltage relationship, we utilize TSE, as its accuracy has been found sufficient in [15]. The quadratic voltage relationship can be approximated by TSE around an operating point f as follows:

$$v_i = f^2 + 2f(u_i - f) + (u_i - f)^2 \quad \forall i \in \mathcal{B}^G \quad (17)$$

where $f \in [\underline{u}_i, \bar{u}_i]$. If the quadratic term in (17) is ignored, it can be approximated as the following linear model:

$$\langle u_i^2 \rangle_{\text{TSE}} \equiv f^2 + 2f(u_i - f) \quad \forall i \in \mathcal{B}^G \quad (18)$$

where the elimination of quadratic term leads to an error whose value depends on the choice of parameter f .

IV. OPTIMAL POWER FLOW FORMULATION

This section presents the DOPF formulation, which integrates the Volt-VAr and Volt-Watt SI functionalities of the PV.

A. Multiperiod DOPF

The dynamic nature of the active distribution network requires that a range of load and solar conditions be considered. Besides, the presence of BESS necessitates a multiperiod DOPF to obtain the optimal dispatch of BESS over the entire time horizon. In this article, a generic BESS model is adopted, which considers a four-quadrant operation capability having the ability to inject and absorb both active and reactive powers during its charging and discharging cycles. The multiperiod DOPF model with BESS requires an intertemporal constraint that couples adjacent time periods, as shown in (19). The use of separate terms for power injected into ($p_{i,\text{CHA}}^{\psi,t}$) or drawn from ($p_{i,\text{DIS}}^{\psi,t}$), the BESS allows for a roundtrip efficiency of less than 100%, which realistically accounts for BESS-to-grid interactions [26].

$$\begin{aligned} \text{SOC}_i^{\psi,t} &= \text{SOC}_i^{\psi,t-1} \\ &- \Delta t \left(\eta_{i,\text{CHAP}}^{\psi,t} p_{i,\text{CHA}}^{\psi,t} + p_{i,\text{DIS}}^{\psi,t} / \eta_{i,\text{DIS}}^{\psi} \right). \end{aligned} \quad (19)$$

The BESS state of charge (SOC), which indicates the available capacity in the BESS, should be maintained within prespecified limits in order to preserve the lifespan of the BESS indicated by (20a). The initial SOC and final SOC are kept the same using (20b). The rate of charging or discharging of the BESS should not exceed its specified rating, as indicated by (20c) and (20d). The use of the binary variables ensures that simultaneous charging and discharging do not occur.

$$\underline{\text{SOC}}_i^{\psi} \leq \text{SOC}_i^{\psi,t} \leq \bar{\text{SOC}}_i^{\psi} \quad (20a)$$

$$\text{SOC}_i^{\psi,1} = \text{SOC}_i^{\psi,T} \quad (20b)$$

$$-\bar{p}_{i,\text{BESS}}^{\psi} b_i^{\psi,t} \leq p_{i,\text{CHA}}^{\psi,t} \leq 0 \quad (20c)$$

$$0 \leq p_{i,\text{DIS}}^{\psi,t} \leq \bar{p}_{i,\text{BESS}}^{\psi} (1 - b_i^{\psi,t}) \quad \forall i \in \mathcal{B}^B \quad \forall \psi \in \Psi_i \quad \forall t \in \mathcal{T}, \quad b_i^{\psi,t} \in \{0, 1\}. \quad (20d)$$

The apparent power of the BESS should limit its active and reactive power capability indicated by

$$\sqrt{(p_{i,\text{CHA}}^{\psi,t} + p_{i,\text{DIS}}^{\psi,t})^2 + (q_{i,\text{BESS}}^{\psi,t})^2} \leq \bar{s}_{i,\text{BESS}}^{\psi} \quad \forall i \in \mathcal{B}^B \quad \forall \psi \in \Psi_i. \quad (21)$$

This nonlinear constraint can be approximated via a 32-vertex polygon [23] as

$$\begin{aligned} -\bar{s}_{i,\text{BESS}}^{\psi} &\leq \cos(l\gamma) (p_{i,\text{CHA}}^{\psi,t} + p_{i,\text{DIS}}^{\psi,t}) + \sin(l\gamma) q_{i,\text{BESS}}^{\psi,t} \\ \bar{s}_{i,\text{BESS}}^{\psi} &\geq \cos(l\gamma) (p_{i,\text{CHA}}^{\psi,t} + p_{i,\text{DIS}}^{\psi,t}) + \sin(l\gamma) q_{i,\text{BESS}}^{\psi,t} \\ \gamma &= \frac{\pi}{k}, \quad l = 1, \dots, k \quad \forall i \in \mathcal{B}^B \quad \forall \psi \in \Psi_i. \end{aligned} \quad (22)$$

B. Objective Function

In the DOPF, different objective functions could be formulated depending on the desired goals to be achieved for optimal dispatch of the DERs as appropriate. Since the *LinDist3Flow* formulation, which is used as the base for the distribution grid model, ignores losses, it would not be ideal to formulate this DOPF problem as a loss minimization problem, although the loss estimation equation in [9] could also be adopted. This article proposes the objective function to minimize the net load curve. This means more significant utilization of the distributed resources (PV and BESS), leading to increased revenues and smoothening the system's net load curve over the entire time horizon. Flattening the net load curve will lead to voltage regulation, thereby improving the power quality, alongside the added benefit of reduced energy costs. The net load can be expressed as

$$\begin{aligned} OF = & \sum_{i \in \mathcal{B}} \sum_{\psi \in \Psi_i} \sum_{t \in \mathcal{T}} p_{i,L}^{\psi,t} - \sum_{i \in \mathcal{B}^G} \sum_{\psi \in \Psi_i} \sum_{t \in \mathcal{T}} p_{i,G}^{\psi,t} \\ & - \sum_{i \in \mathcal{B}^B} \sum_{\psi \in \Psi_i} \sum_{t \in \mathcal{T}} p_{i,\text{CHA}}^{\psi,t} - \sum_{i \in \mathcal{B}^B} \sum_{\psi \in \Psi_i} \sum_{t \in \mathcal{T}} p_{i,\text{DIS}}^{\psi,t}. \end{aligned} \quad (23)$$

C. DOPF Model

An unbalanced three-phase multiperiod DOPF model that incorporates $\mathbf{Q}(\mathbf{V})$ and $\mathbf{P}(\mathbf{V})$ droops is obtained by integrating the BESS model (19)–(22), and the copy of static constraints (1)–(18) for each time period.

Minimize (23)

Subject to :

Constraints (1)–(22) $\forall t \in \mathcal{T}$.

Note that although this formulation utilizes a convex grid model, the introduction of discrete variables in the piecewise modeling of the droop curves and BESS model makes the formulation become MILP, which is inherently nonconvex.

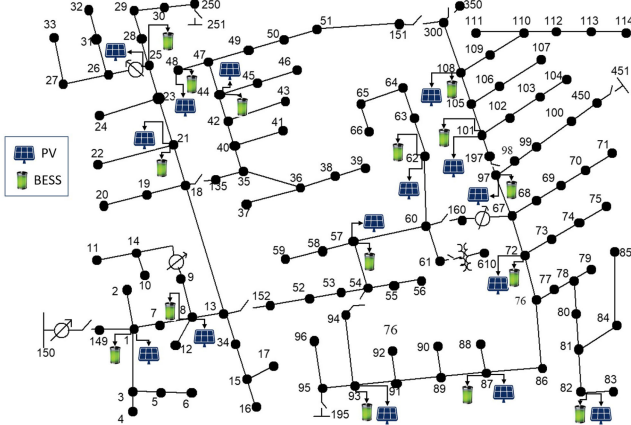


Fig. 4. IEEE 123-bus distribution feeder with PV and BESS.

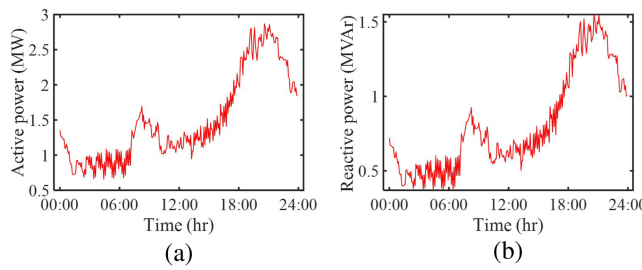


Fig. 5. Total loads. (a) Active power profile. (b) Reactive power profile.

V. TEST SYSTEM SETUP AND CASE STUDIES

A. Test System Setup

The IEEE 123-node three-phase feeder [27] is used to validate the effectiveness of the DOPF formulation. Voltage regulators are disabled, and switches are modeled as open/shorted lines depending on their status. Distributed loads are ignored, and all spot loads are modeled as constant power loads with a wye connection. Line shunt parameters are ignored, as lines in distribution systems are typically short that the shunt admittance can be neglected [24]. Capacitor banks are modeled as constant reactive power sources. The substation node is fixed to the nominal system voltage of 1 p.u.

Integrated into the IEEE 123-bus feeder are 15 PVs and BESS with the locations shown in Fig. 4. The PVs and BESS are colocated and coupled on the ac side such that each has its independent inverter. Each PV system has an active power rating of 300 kW. Each BESS system is rated 2 MW/20 MWh and restricted between 10% and 85% of the maximum SOC to preserve the BESS lifetime. The BESS operates at an inverter efficiency of 95% with an initial SOC and final SOC of 10 MWh. Both PV and BESS systems have an oversized SI, such that the apparent power capacity is 110% of the active power rating, which enables the SI to absorb/inject reactive power without affecting the active power generation. Fig. 5 shows aggregate active and reactive power loads with 5-min resolution (288 time slots) on a typical day. Two PV profiles, as shown in Fig. 6, are used, which correspond to cloudy and sunny days, respectively.

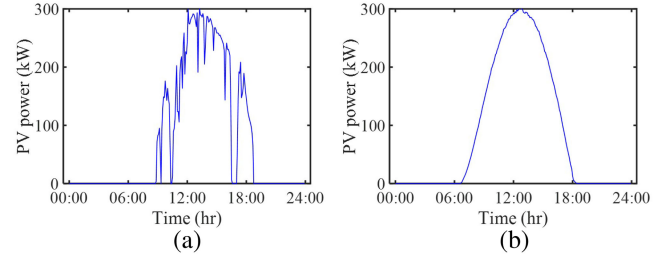


Fig. 6. PV profiles. (a) Cloudy day. (b) Sunny day.

Based on the IEEE-1547 defined range of SI settings, the following voltage breakpoints are selected for $\mathbf{Q}(\mathbf{V})$ droops: $\{0.9, 0.92, 0.98, 1.02, 1.08, 1.1\}$ p.u. Voltage breakpoints for the $\mathbf{P}(\mathbf{V})$ are chosen as $\{0.9, 1.0, 1.06, 1.1\}$ p.u. Note that $w = 6$ for the $\mathbf{Q}(\mathbf{V})$ droop, and $w = 4$ for $\mathbf{P}(\mathbf{V})$ droop. The SI droop functionalities are enabled and only capable of reactive power support when the SI is online during available active power generation in accordance with IEEE-1547. The maximum reactive power injection/absorption that each SI can provide is set to 44% of the SI's apparent power rating, which is equivalent to operating at 0.9 power factor at full output [28]. The MILP-DOPF model is solved using the Gurobi solver in JuMP [29] modeling environment.

B. Case Studies

During the simulation, the following test case scenarios are considered.

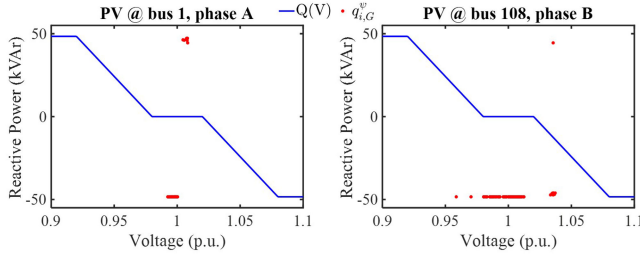
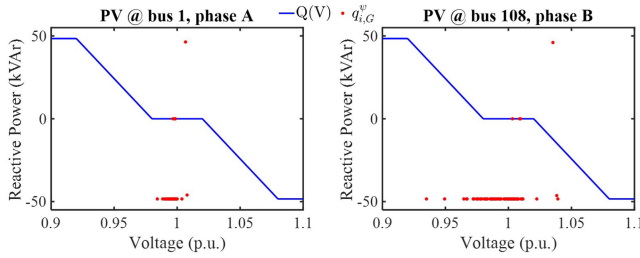
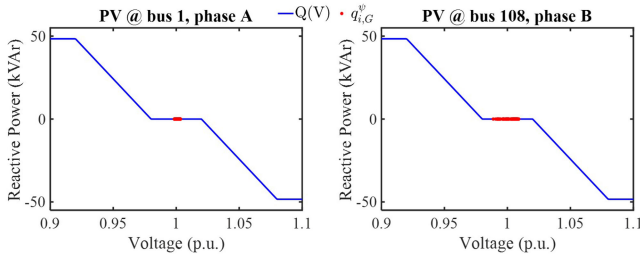
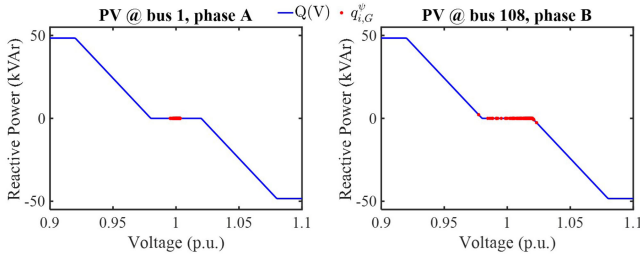
- 1) *Case 1:* With PV only (both Volt-Watt and Volt-VAr SI functionalities enabled) during a sunny day.
- 2) *Case 2:* With PV only (both Volt-Watt and Volt-VAr SI functionalities enabled) during a cloudy day.
- 3) *Case 3:* With PV (both Volt-Watt and Volt-VAr SI functionalities enabled) and BESS model included during a sunny day.
- 4) *Case 4:* With PV (both Volt-Watt and Volt-VAr SI functionalities enabled) and BESS model included during a cloudy day.

VI. SIMULATION RESULTS AND ANALYSIS

A. Reactive Power and Voltage Performance With and Without $\mathbf{Q}(\mathbf{V})$ Droop

First, we show the motivation for incorporating $\mathbf{Q}(\mathbf{V})$ droop function as a constraint into the DOPF model. Dispatching SI reactive power setpoints without consideration of the droop curve might lead to dispatch solutions that do not lie on the droop curve, akin to approaches used in [9]–[11]. This would render the DOPF-based solution unsuitable at the local control level. This is shown in Figs. 7 and 8, which show that the reactive power dispatch of SIs at phase A of bus 1 and phase B of bus 108 (for cases 1 and 2) do not lie on $\mathbf{Q}(\mathbf{V})$ droop lines.

On the other hand, the effectiveness of the proposed approach is illustrated by how the reactive power dispatch solution obtained from the proposed DOPF model lies on the $\mathbf{Q}(\mathbf{V})$ droop.

Fig. 7. Reactive power dispatch without $\mathbf{Q}(\mathbf{V})$ droop for case 1.Fig. 8. Reactive power dispatch without $\mathbf{Q}(\mathbf{V})$ droop for case 2.Fig. 9. Reactive power dispatch with $\mathbf{Q}(\mathbf{V})$ for case 1.Fig. 10. Reactive power dispatch with $\mathbf{Q}(\mathbf{V})$ for case 2.

Figs. 9 and 10 show the reactive power dispatch when $\mathbf{Q}(\mathbf{V})$ droop function is modeled as a constraint in the DOPF for cases 1 and 2. Unlike the DOPF models in [9]–[11], our reactive power setpoints lie precisely on the $\mathbf{Q}(\mathbf{V})$ droops, showing the effectiveness of the proposed DOPF model in abiding by the IEEE-1547 standard and therefore suitable at the local inverter controller level.

Furthermore, as can be seen from Fig. 11, for case 1, the distribution of bus voltages without $\mathbf{Q}(\mathbf{V})$ droop has a more significant standard deviation (0.02532 p.u.) compared to that with the droop (0.014369 p.u.). Thus, integrating droops into

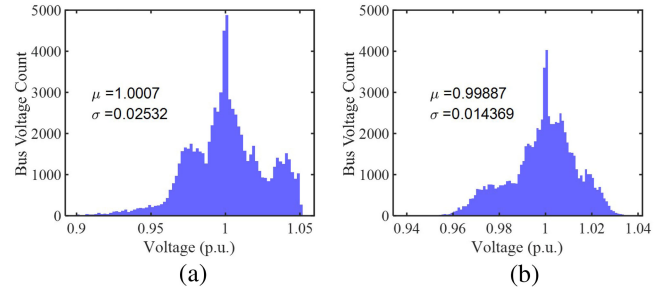
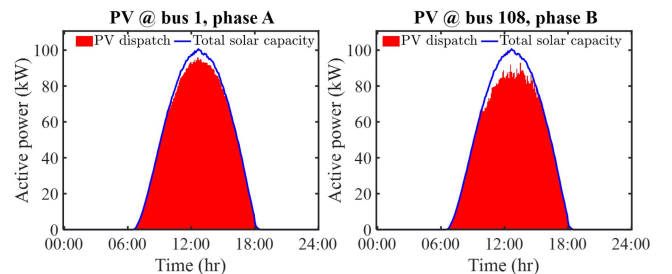
Fig. 11. Voltage histogram for case 1. (a) Without $\mathbf{Q}(\mathbf{V})$ droop. (b) With $\mathbf{Q}(\mathbf{V})$ droop.

Fig. 12. Active power dispatch with total solar capacity for case 1.

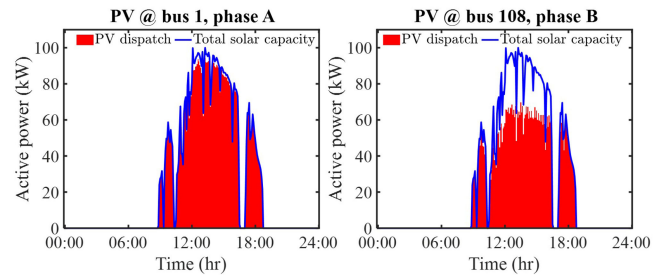


Fig. 13. Active power dispatch with total solar capacity for case 2. (a) PV at bus 1, phase A. (b) PV at bus 108, phase B.

the DOPF model is imperative for effective voltage control in distribution feeders where slight bus voltage variance is desired.

B. PV Utilization Performance

One major challenge associated with the huge uptake of solar technologies stems from the fact that peak PV production does not often coincide with peak demand. For example, peak PV production occurs at 12:50 P.M. on the sunny day (as shown in Fig. 6), while peak demand occurs at 8:40 P.M. (as shown in Fig. 5). This peak PV generation can lead to overgeneration, since there might be no demand for it at that time. This subsequently forces system operators to curtail the PV generation, reducing its economic and environmental benefits, as shown in Figs. 12 and 13 for cases 1 and 2, respectively.

Figs. 14 and 15 show the active power dispatch relative to the $\mathbf{P}(\mathbf{V})$ droop for cases 1 and 2, respectively. It can be seen from the figures that the entire PV generation lies under the defined $\mathbf{P}(\mathbf{V})$ curve, which is added as a constraint of

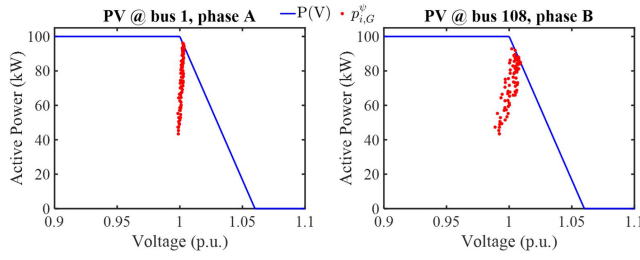


Fig. 14. Active power dispatch with total solar capacity for case 1. (a) PV at bus 1, phase A. (b) PV at bus 108, phase B.

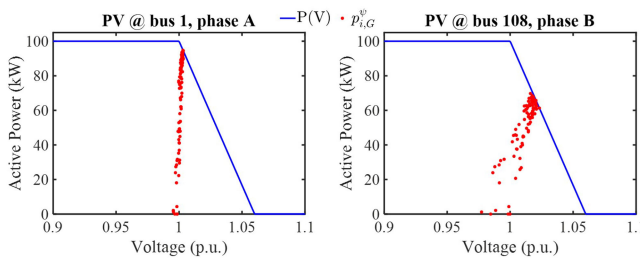


Fig. 15. Active power dispatch with total solar capacity for case 2.

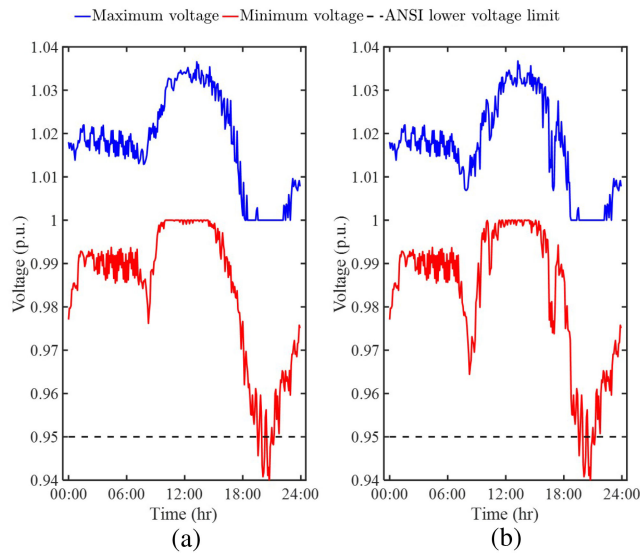


Fig. 16. Maximum and minimum voltage during the following. (a) Case 1. (b) Case 2.

the proposed DOPF formulation. This ensures that the active power dispatch lies under the predefined $\mathbf{P}(\mathbf{V})$ according to the IEEE 1547 standard. Moreover, the maximum active power capacity changes per time based on the available solar irradiance, accounting for the active power setpoints dispatched under the area of the $\mathbf{P}(\mathbf{V})$ curve.

It is also worth noting that even though the PV curtailment eliminates any overvoltage issue, there is still an undervoltage problem, as shown in Fig. 16, due to the inability of the PV system to participate in voltage regulation after the sun has set during peak demand.

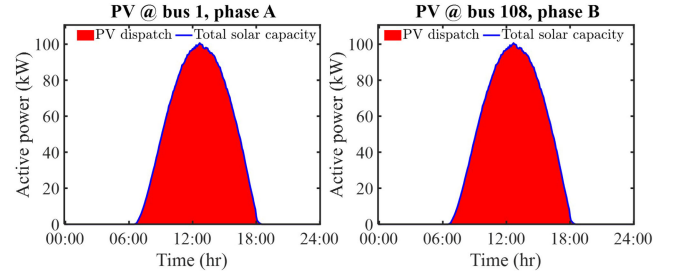


Fig. 17. Active power dispatch with total solar capacity for case 3.

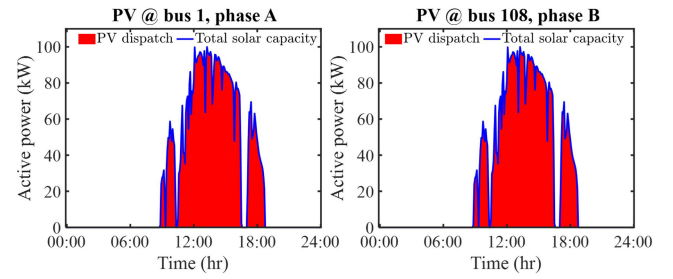


Fig. 18. Active power dispatch with total solar capacity for case 4.

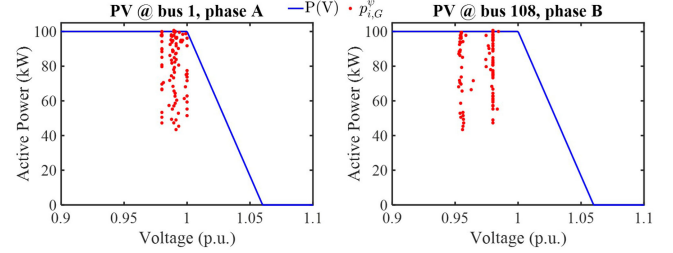


Fig. 19. Active power dispatch on $\mathbf{P}(\mathbf{V})$ droop for case 3.

C. BESS Utilization Performance

The uptake of solar technologies increases the need for other generating sources to rapidly ramp up energy production after sunset when the PV system no longer generates energy, leading to a nonsmooth net load. One solution to alleviate this situation is the use of PV coupled with storage technologies. Figs. 17 and 18 show that the PV is better utilized when BESS is installed for cases 3 and 4, respectively, with very little to no curtailment as the excess energy can be stored in the BESS for use during the peak demand period. Storage could therefore enhance reliance on solar energy to balance supply and demand on the grid.

Figs. 19 and 20 show the active power dispatch relative to the $\mathbf{P}(\mathbf{V})$ droop for cases 3 and 4, respectively. As previously established, these figures further illustrate that the inclusion of the BESS improves the utilization of the PV.

The objective function values (net load) after solving the optimization model during cases 1–4 are 130.34, 168.39, 97.19, and 118.22 MW, respectively. Fig. 21 compares the net load for cases 1 and 3, while Fig. 22 compares the net load for cases 2 and 4. Notice that in Figs. 21(a) and 22(a), the curve dips significantly around 8:50 A.M., and then drastically increases at

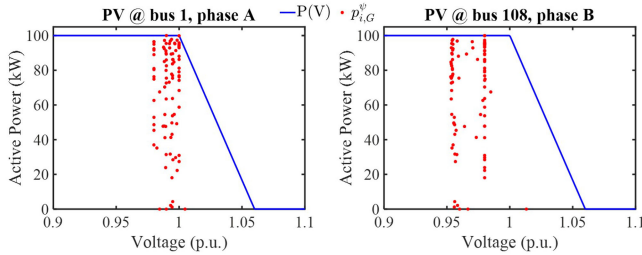
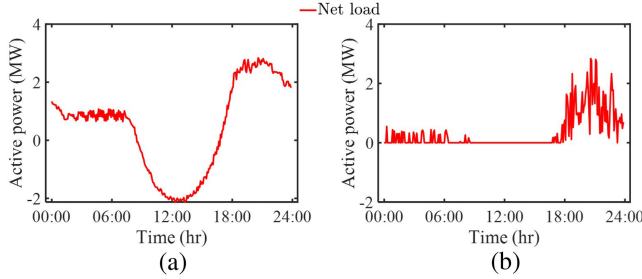
Fig. 20. Active power dispatch on $\mathbf{P}(V)$ droop for case 4.

Fig. 21. Net load curve during the following. (a) Case 1. (b) Case 3.

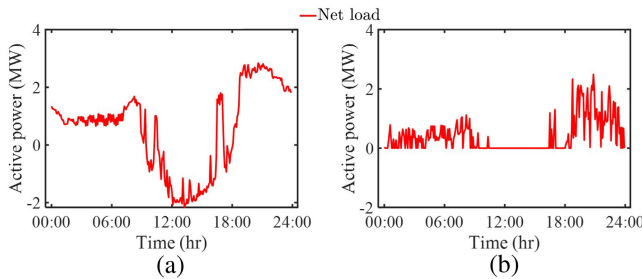


Fig. 22. Net load curve during the following. (a) Case 2. (b) Case 4.

7:10 P.M. With the installation of BESS infrastructure, however, this issue associated with solar abundance during the day is mitigated, as shown in Figs. 21(b) and 22(b). Storing excess solar power during the day and utilizing it in the evening can help to reduce the disparity between inexpensive midday and expensive evening energy prices. The variability index (VI) can be used to assess the level of variations in net load in daily optimization as follows:

$$VI = \frac{\sigma_v^2}{|\mu_v|} \times 10^4 \quad (24)$$

where σ_v^2 is the variance and μ_v is the mean of the daily net load profile. In scenarios without BESS (cases 1 and 2), the VIs are 1.59 and 1.71, respectively, whereas with the BESS (cases 3 and 4), the VIs are 0.16 and 0.27, respectively. Hence, a smoother net load profile is achieved with the inclusion of BESS.

The BESS charging and discharging profiles are shown in Fig. 24(a), with the corresponding SOC profile illustrated in Fig. 24(b). Since there is an initial SOC at the start of the cycle, discharging first occurs between 6:20 and 8:10 A.M. when the sun is just starting to rise. As more solar power becomes generated

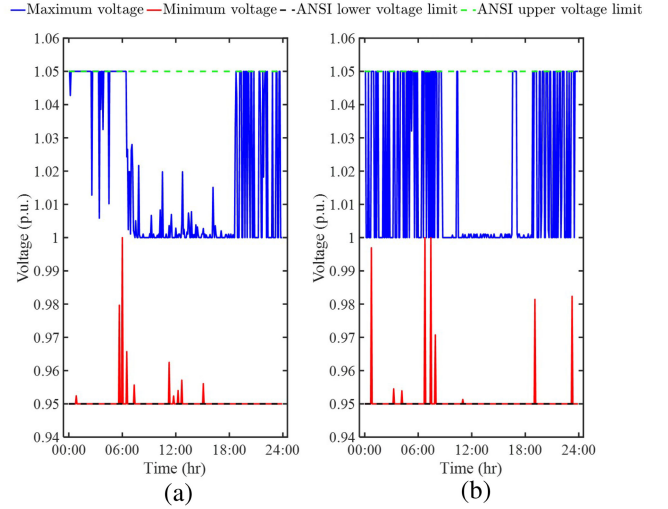


Fig. 23. Maximum and minimum voltage during the following. (a) Case 3. (b) Case 4.

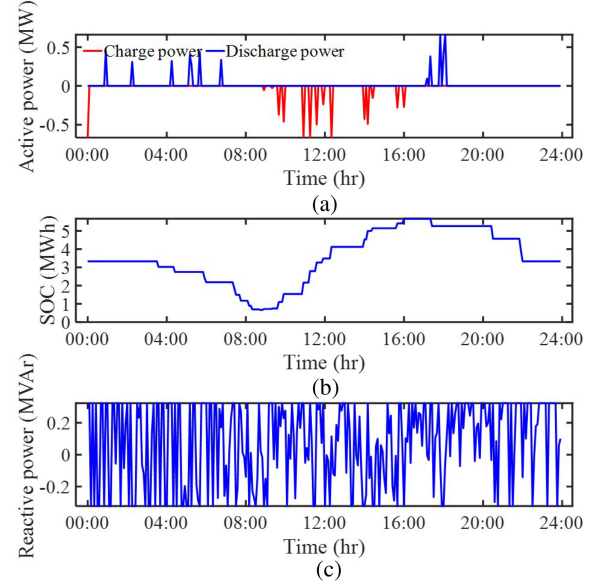


Fig. 24. BESS at bus 108, phase A for case 3. (a) BESS active power flow. (b) BESS SOC. (c) BESS reactive power flow.

and load demand decreases, the BESS charges between 11:50 A.M. and 5:40 P.M. Finally, the BESS discharges between 9:40 P.M. till the end of the day, since solar power is no longer available and load demand is relatively high during this time period. The BESS also provides reactive power support, as shown in Fig. 24(c). Also, the BESS provides the necessary voltage regulation support, as shown in Fig. 23.

D. Evaluation of Accuracy of First-Order Voltage Approximation Method

In the simulation, TSE parameter is set to $f = (\underline{u}_i + \bar{u}_i)/2$. To evaluate the accuracy of the TSE first-order voltage approximation, we obtain the approximation errors during all

cases analyzed. The mismatch between $\sqrt{v_i^\psi}$ and u_i^ψ can be quantified with the average relative error calculated over all the PV-connected nodes for daily simulation as follows:

$$\text{Err}^t = \frac{1}{|\mathcal{B}^G|} \sum_{i \in \mathcal{B}^G} \sum_{\psi \in \Psi_i} \left| \frac{\sqrt{v_i^{\psi,t}} - u_i^{\psi,t}}{\sqrt{v_i^{\psi,t}}} \right| 100\% \quad \forall t \in \mathcal{T}. \quad (25)$$

We also obtain a compact error metric by averaging all Err^t over the optimization horizon as

$$\text{ERR} = \frac{1}{\mathcal{T}} \sum_{t \in \mathcal{T}} \text{Err}^t. \quad (26)$$

The errors introduced by the voltage approximation for cases 1–4 are 0.032%, 0.029%, 0.174%, and 0.215%, respectively. Hence, the TSE provides a satisfactory approximation between $u_i^{\psi,t}$ and $\sqrt{v_i^{\psi,t}}$.

VII. CONCLUSION

This article presented an efficient MILP DOPF formulation incorporating Volt-VAr and Volt-Watt droop functions in an unbalanced DOPF model. The need for this DOPF model was motivated by the growing integration of PV systems in distribution networks, coupled with requirements for droop-based inverter control as per the IEEE-1547 standard. The proposed DOPF model was based on the well-known *LinDist3Flow* formulation and mixed-integer linear reformulation of Volt-VAr and Volt-Watt droop curves of the SIs. Case studies demonstrated that dispatch solutions lie precisely on the droop curves showing the effectiveness of the proposed model in obtaining SI setpoints that abide by the IEEE-1547 standard. The proposed formulation has desirable application in efficient voltage regulation and load-leveling applications as measured by the VI. We showed that the proposed MILP model is efficient by solving the formulation on the IEEE 123-node feeder, making it to be quite promising for practical-sized feeders. Along with a generic BESS model, the droop-integrated DOPF model was also shown to provide voltage regulation support and minimize active power curtailment. Future work will explore efficient schemes to design optimal SI settings and modes to mitigate voltage violations in multiphase networks and integrate the SI droop model of BESS into the DOPF framework.

REFERENCES

- [1] IRENA, “Renewable capacity statistics 2021,” Int. Renewable Energy Agency, Abu Dhabi, UAE, Tech. Rep., 2021.
- [2] F. Katiraei and J. R. Agüero, “Solar PV integration challenges,” *IEEE Power Energy Mag.*, vol. 9, no. 3, pp. 62–71, May/Jun. 2011.
- [3] *IEEE Standard for Interconnection and Interoperability of Distributed Energy Resources With Associated Electric Power Systems Interfaces*, IEEE Standard 1547–2018, 2018.
- [4] J. T. Johnson, “Draft electric rule 21 test protocols for advanced inverter functions,” *Sandia Nat. Lab.*, Albuquerque, NM, USA, Tech. Rep., 2014.
- [5] Rule no. 14, “Service connections and facilities on customer’s premises, hawaiian electric.” Accessed: Jun. 16, 2022. [Online]. Available: https://www.hawaiianelectric.com/documents/billing_and_payment/rates/hawaiian_electric_rules/14.pdf
- [6] A. Singhal, V. Ajjarapu, J. Fuller, and J. Hansen, “Real-time local volt/var control under external disturbances with high PV penetration,” *IEEE Trans. Smart Grid*, vol. 10, no. 4, pp. 3849–3859, Jul. 2019.
- [7] B. Seal and B. Ealey, “Common functions for smart inverters, 4th ed.,” Electric Power Res. Inst., Washington, DC, USA, Tech. Rep. 3002008217, 2016.
- [8] A. Inaojali, A. Savasci, and S. Paudyal, “Distribution grid optimal power flow with Volt-VAr and Volt-Watt settings of smart inverters,” in *Proc. IEEE Ind. Appl. Soc. Annu. Meeting*, 2021, pp. 1–7.
- [9] K. Turitsyn, P. Sulc, S. Backhaus, and M. Chertkov, “Options for control of reactive power by distributed photovoltaic generators,” *Proc. IEEE*, vol. 99, no. 6, pp. 1063–1073, Jun. 2011.
- [10] M. Farivar, R. Neal, C. Clarke, and S. Low, “Optimal inverter VAR control in distribution systems with high PV penetration,” in *Proc. IEEE Power Energy Soc. Gen. Meeting*, 2012, pp. 1–7.
- [11] X. Su, M. A. S. Masoum, and P. J. Wolfs, “Optimal PV inverter reactive power control and real power curtailment to improve performance of unbalanced four-wire LV distribution networks,” *IEEE Trans. Sustain. Energy*, vol. 5, no. 3, pp. 967–977, Jul. 2014.
- [12] R. Shan, A. Abdulla, and M. Li, “Deleterious effects of strategic, profit-seeking energy storage operation on electric power system costs,” *Appl. Energy*, vol. 292, 2021, Art. no. 116833.
- [13] D. K. Molzahn and I. A. Hiskens, *A Survey of Relaxations and Approximations of the Power Flow Equations*. Delft, The Netherlands: Now Publishers, 2019.
- [14] P. Lusis, L. L. Andrew, A. Liebman, and G. Tack, “Interaction between coordinated and droop control PV inverters,” in *Proc. 11th ACM Int. Conf. Future Energy Syst.*, 2020, pp. 314–324.
- [15] A. Savasci, A. Inaojali, and S. Paudyal, “Distribution grid optimal power flow integrating volt-var droop of smart inverters,” in *Proc. IEEE Green Technol. Conf.*, 2021, pp. 54–61.
- [16] T. O. Olowu, A. Inaojali, A. Sarwat, and S. Paudyal, “Optimal Volt-VAR and Volt-Watt droop settings of smart inverters,” in *Proc. IEEE Green Technol. Conf.*, 2021, pp. 89–96.
- [17] T. M. Aljohani, A. Saad, and O. A. Mohammed, “Two-stage optimization strategy for solving the VVO problem considering high penetration of plug-in electric vehicles to unbalanced distribution networks,” *IEEE Trans. Ind. Appl.*, vol. 57, no. 4, pp. 3425–3440, Jul./Aug. 2021.
- [18] Mosk Modeling Cookbook 3.2.2, Accessed: May 3, 2021. [Online]. Available: <https://docs.mosek.com/modeling-cookbook/mio.html>
- [19] M. D. Sankur, R. Dobbe, E. Stewart, D. S. Callaway, and D. B. Arnold, “A linearized power flow model for optimization in unbalanced distribution systems,” 2016, *arXiv:1606.04492*.
- [20] A. Inaojali, A. Savasci, S. Paudyal, and S. Kamalasadan, “Accuracy of phase-decoupled and phase-coupled distribution grid power flow models,” in *Proc. IEEE Power Energy Soc. Innov. Smart Grid Technol. Conf.*, 2021, pp. 1–5.
- [21] A. Savasci, A. Inaojali, and S. Paudyal, “Distribution grid optimal power flow with adaptive Volt-VAr droop of smart inverters,” in *Proc. IEEE Ind. Appl. Soc. Annu. Meeting*, 2021, pp. 1–8.
- [22] A. Inaojali, A. Savasci, and S. Paudyal, “Optimal droop settings of smart inverters,” in *Proc. IEEE 48th Photovolt. Specialists Conf.*, 2021, pp. 2584–2589.
- [23] R. A. Jabr, “Linear decision rules for control of reactive power by distributed photovoltaic generators,” *IEEE Trans. Power Syst.*, vol. 33, no. 2, pp. 2165–2174, Mar. 2018.
- [24] W. H. Kersting, *Distribution System Modeling and Analysis*. Boca Raton, FL, USA: CRC Press, 2018.
- [25] L. Gan and S. H. Low, “Convex relaxations and linear approximation for optimal power flow in multiphase radial networks,” in *Proc. Power Syst. Computation Conf.*, 2014, pp. 1–9.
- [26] A. Castillo and D. F. Gayme, “Grid-scale energy storage applications in renewable energy integration: A survey,” *Energy Convers. Manage.*, vol. 87, pp. 885–894, 2014.
- [27] K. P. Schneider *et al.*, “Analytic considerations and design basis for the IEEE distribution test feeders,” *IEEE Trans. Power Syst.*, vol. 33, no. 3, pp. 3181–3188, May 2018.
- [28] M. Rylander, H. Li, J. Smith, and W. Sunderman, “Default volt-var inverter settings to improve distribution system performance,” in *Proc. IEEE Power Energy Soc. Gen. Meeting*, 2016, pp. 1–5.
- [29] J. Bezanson, A. Edelman, S. Karpinski, and V. B. Shah, “Julia: A fresh approach to numerical computing,” *SIAM Rev.*, vol. 59, no. 1, pp. 65–98, 2017.



Adedoyin Inaolaji (Graduate Student Member, IEEE) received the B.Eng. degree in electrical and electronics engineering from Covenant University, Ota, Nigeria, in 2014, and the M.Sc. degree in electrical engineering in 2022 from the Department of Electrical and Computer Engineering, Florida International University, Miami, FL, USA, where she is currently working toward the Ph.D. degree in electrical engineering.

Her research interests include distribution grid modeling, analysis, and optimization techniques.



Sumit Paudyal (Member, IEEE) received the B.E. degree from Tribhuvan University, Kirtipur, Nepal, in 2003, the M.Sc. degree from the University of Saskatchewan, Saskatoon, SK, Canada, in 2008, and the Ph.D. degree from the University of Waterloo, Waterloo, ON, Canada, in 2012, all in electrical engineering.

From 2012 to 2019, he was a Faculty Member with Michigan Technological University, Houghton, MI, USA. Since 2019, he has been an Associate Professor with the Department of Electrical and Computer

Engineering, Florida International University, Miami, FL, USA. His research interests include distribution grid modeling, dynamic studies, and optimization techniques in power systems.



Alper Savasci (Graduate Student Member, IEEE) received the B.S. degree in electrical and electronics engineering from Erciyes University, Kayseri, Turkey, in 2012, and the M.Sc. degree in electrical engineering from Michigan Technological University, Houghton, MI, USA, in 2018. He is currently working toward the Ph.D. degree in electrical engineering from Florida International University, Miami, FL, USA.

His research interests include distribution system modeling and optimization.